



Photocatalysts fabricated by depositing plasmonic Ag nanoparticles on carbon quantum dots/graphitic carbon nitride for broad spectrum photocatalytic hydrogen generation

Jiayi Qin ^a, Heping Zeng ^{a,b,*}

^a *Guangzhou Key Laboratory of Materials for Energy Conversion and Storage, School of Chemistry and Environment, South China Normal University, Guangzhou, 510006, PR China*

^b *State Key Laboratory of Luminescent Materials and Devices, Institute of Functional Molecules, School of Chemistry and Chemical Engineering, South China University of Technology, Guangzhou, 510641, PR China*



ARTICLE INFO

Article history:

Received 15 October 2016

Received in revised form 16 January 2017

Accepted 1 March 2017

Available online 2 March 2017

Keywords:

Graphitic carbon nitride

Upconversion

Plasmonic silver

Broad spectrum

Hydrogen generation

ABSTRACT

To make the best and highest use of broad spectrum solar energy remains a tremendous challenge and the main target in the photocatalytic area. A novel promising photocatalyst supported on surface plasmon resonance of Ag nanoparticles (NPs) and upconversion photoluminescence property from carbon quantum dots (CQDs) is reported to improve broad spectrum absorption and photoinduced charge transfer of graphitic carbon nitride ($g\text{-C}_3\text{N}_4$) in the photo-driven H_2 production for the first time. Here the new-styled nanocomposites not only have more prominent UV-vis photocatalytic ability, also can harness near-infrared light to trigger hydrogen evolution in aqueous solution. Meanwhile, Ag NPs and CQDs serve as electron-reservoirs, which stimulate the separation of photo-generated electron-holes, enhancing quantum efficiency of $g\text{-C}_3\text{N}_4$. Remarkably, the most notable photocatalytic hydrogen generation as high as $626.93 \mu\text{mol g}^{-1} \text{h}^{-1}$ under visible light, which is about 6.7 and 2.8 times higher than pure $g\text{-C}_3\text{N}_4$ and the best CQDs/ $g\text{-C}_3\text{N}_4$ composite respectively, was achieved upon 6 mL CQDs/ $g\text{-C}_3\text{N}_4$ (6CCN) loaded with 3 wt% Ag. Moreover, a facile method is designed to prepare Ag/CQDs/ $g\text{-C}_3\text{N}_4$ photocatalysts, and their chemical composition, morphologies, optical properties and stability were characterized methodically.

© 2017 Elsevier B.V. All rights reserved.

1. Introduction

The exploitation and establishment of efficient, innocuous and sustainable semiconductor photocatalysts, devoted to solar power conversion into hydrogen fuel, is a fascinating science and urgently need to be addressed issue in the 21st century, with the aggravation of energy depletion and environmental crises [1–5]. For the past few years, graphitic carbon nitride ($g\text{-C}_3\text{N}_4$), one of the most emphasized photocatalysts, has been widely applied in solar-initiated hydrogen production from water or water solution, photo-reduction of CO_2 and organic contaminants, NO_x decomposition and oxygen activation sites identification [6–11]. This organic polymeric photocatalyst is consisted of tri-s-triazine planar units that only contain carbon and nitrogen, which are earth-abundant elements and can be simply acquired

via directly calcining nitrogen-rich precursors [10–12]. Additionally, the π -conjugated graphene-like porous structure ensures it extraordinary endurance in rigorous experimental conditions and certain electronic properties for charge transfer [13,15]. As a visible light active semiconductor, $g\text{-C}_3\text{N}_4$ also has a relatively narrow band gap of 2.7 eV and appropriate conduction band and valence band, which is suitable for absorbing UV-vis light with wavelength less than 460 nm for H_2 evolution [16]. However, the blue light that $g\text{-C}_3\text{N}_4$ only can absorb accounts for a very small proportion in the full solar spectrum, resulting in the unavailability of more visible light and infrared light ($\sim 53\%$) with lower energy in sunshine [11,17,18]. Besides, poor charge mobility, rapid charge recombination and low surface area also impose serious restriction on the photocatalytic performance of $g\text{-C}_3\text{N}_4$ [19–21]. There have been many efforts put into addressing these issues, for instance, forming heterojunction between $g\text{-C}_3\text{N}_4$ and organic or inorganic semiconductors to adjust the band gap [12,20,22–24], doping metal/non-metal or carbon nanomaterials for improving visible light absorption and photoelectrons migration [25–27]. Likewise, sensitization by organic dyes or quantum dots and morphological

* Corresponding author at: State Key Laboratory of Luminescent Materials and Devices, Institute of Functional Molecules, School of Chemistry and Chemical Engineering, South China University of Technology, Guangzhou, 510641, PR China.

E-mail address: hpzeng@scut.edu.cn (H. Zeng).

design both contribute to boosting light utilization efficiency and quantum yield of $g\text{-C}_3\text{N}_4$ [10,28–30]. Nevertheless, there is still a lack of strategies to assist $g\text{-C}_3\text{N}_4$ to utilize broad spectrum, and even near-infrared light.

Loading noble metal nanoparticles onto the semiconductor surfaces was proved to be beneficial to extend the light-harvesting scope in visible light for producing more e_{CB}^- - h_{VB}^+ pairs by virtue of strong electromagnetic field formed by localized surface plasmon resonance (LSPR) [31–33]. Meanwhile, Schottky junction at the interface can also prevent the recombination of photo-generating carrier and maintain the reducibility of transferred electrons [34,35]. Besides, among the noble metals, Ag nanoparticles have the cheapest raw materials and the strongest LSPR effect [36]. Recently, Ag loaded $g\text{-C}_3\text{N}_4$ as a catalyst has been popular in many areas. Chen et al. discovered a one-step mix-calcination method to prepare Ag quantum dots/ $g\text{-C}_3\text{N}_4$ composite applied in photocatalytic water splitting, and the maximum visible-light-driven hydrogen production efficiency was raised by 4.6 times compared with $g\text{-C}_3\text{N}_4$ [37]. With Ag NPs homogeneously dispersed $g\text{-C}_3\text{N}_4$ was utilized in photodegrading methylene blue by Faisal et al. in recent time, and the highest photodegradation rate almost tripled over the pure $g\text{-C}_3\text{N}_4$ [25]. In the photocatalytic disinfection application, both Ma et al. [35] and Batista et al. [38] found that Ag-modified $g\text{-C}_3\text{N}_4$ composite has excellent bactericidal activity against *Escherichia coli* upon UV and visible light excitation, due to the semiconductor-metal heterojunction effect on light absorption and charges separation. Sun et al. take advantage of Ag/ $g\text{-C}_3\text{N}_4$ photocatalysts to remove NO_x in the air under visible light irradiation illumination [39] and the study of Wang et al. showed Ag and $g\text{-C}_3\text{N}_4$ were also appropriate for electrochemiluminescence detection of cancer cells [40]. In addition, Ag nanoparticles usually act as bridges to simultaneously connect $g\text{-C}_3\text{N}_4$ and another semiconductor or an electrons sink attached to a $g\text{-C}_3\text{N}_4$ -semiconductor structure in a three-component photocatalyst for more optimal photocatalytic performance [36,41–43]. Based on the aforementioned reports and our previous research [6,38,44], in the UV-vis diffuse reflectance spectra, Ag/ $g\text{-C}_3\text{N}_4$ nanocomposites exhibited intense surface plasmon resonance from 410 nm to 550 nm as a result of the introduction of silver nanoparticles. Hence, the absence of the longer wavelength light utilization is the biggest imperfection toward the photocatalyst, which needs to be promptly resolved in the future.

As we all know, carbon quantum dots (CQDs), a novel class of recently developed inexpensive quasi-spherical nanocarbon particles with diameter less than 10 nm [45,46], have exerted its huge application prospects in fluorescence and electrochemical detection [47,48], biological sensing and imaging [49,50], chemiluminescence materials [51] and photo-, photoelectrochemical catalysis [52,53], owing to conspicuous water-solubility and biocompatibility [45,47], avirulence [50], favorable electrical conductivity [49], reducibility [9], and stable photoluminescence that depends on size and excitation wavelength [51]. Especially in photocatalysis aspect, CQDs not only simultaneously own down- and up-conversion PL, which endow them the possibility to campaign as photosensitizers for capturing visible and NIR light, but also work as an electronic buffer to accept or provide electrons for the contiguous semiconductor [17,54]. Posteriorly, π -conjugated structure and oxygen-containing groups at the surface render CQDs photostability and easy-complexation with semiconductors and metal nanoparticles. In this regard, CQDs-based photocatalytic systems such as CQDs/TiO₂ [17], CQDs/ZnS [50], CQDs/Cu₂O [55], CQDs/H- γ -TaON [56], CQDs/Bi₄O₅I₂ [57], CQDs/Ni-complex [58] have demonstrated their remarkable photocatalytic H₂ evolution and photodegrade abilities utilizing wide spectrum. Liu et al. was the first to introduce CQDs into $g\text{-C}_3\text{N}_4$ by electrochemical synthesis and calcination, then in the photocatalytic solar water splitting,

the resultant 2.0% STH efficiency reached the highest than any stable water-splitting photocatalysts reported before [59]. Later, Fang et al. fabricated carbon dots modified $g\text{-C}_3\text{N}_4$ by collecting combustion soot of an alcohol burner followed by calcination the mixture of C-dots and dicyandiamide, finally, the highest H₂ evolution rate (HER) is almost 2.4 times increased than pristine $g\text{-C}_3\text{N}_4$ under visible light irradiation [60]. Soon afterwards, Li et al. developed CQDs-doped $g\text{-C}_3\text{N}_4$ nanosheets (CNNS), which obtained by annealing dicyandiamide to form $g\text{-C}_3\text{N}_4$ firstly, and then thermal treatment of citric acid-6-aminohexanoic acid Na as precursors to get CQDs, lastly they are mixed for further solvothermal reaction. The CNNS/CQDs composite displays the highest photocatalytic H₂ production rate of 116.1 $\mu\text{mol g}^{-1} \text{h}^{-1}$ in visible light [61]. As for as CQDs/metal nanoparticles (such as Au, Ag, Cu), there has been no researches about their application in photocatalytic H₂ generation except in the sensor and photocatalytic cyclohexane oxidation [62,63]. Until 2014, Liu et al. considered that the combination of Ag, CQDs with POMs might be a special approach to construct an efficient and stable photocatalyst for solar water splitting, leading to the active region extended to 650 nm and apparent quantum yield reached 4.9% at 480 nm [44]. However, doping both Ag NPs and CQDs concurrently onto $g\text{-C}_3\text{N}_4$ for photocatalysis remains a vacancy.

In this work, in light of the SPR effect of silver NPs, up-converting PL property of CQDs, and visible light driven H₂ production ability of $g\text{-C}_3\text{N}_4$, Ag/CQDs/ $g\text{-C}_3\text{N}_4$ complex photocatalysts were designed and fabricated here without precedent. In UV and visible light with wavelengths shorter than 550 nm region, Ag nanoparticles exhaust ability to capture photons provided to $g\text{-C}_3\text{N}_4$ for electronic transition. Upon NIR and visible light with wavelengths more than 550 nm irradiation, CQDs become the dominant component to play a major role to transfer energy from long wavelengths light to visible light, which could be absorbed by $g\text{-C}_3\text{N}_4$ to initiate the next photocatalytic reactions, ameliorating the broad spectrum catalytic competence. The best as-prepared heterostructure exhibits the desired HER performance and photostability in visible light, and even the 900 nm NIR light. Apart from this, the synthesis method we reported is comparatively uncomplicated and saving time and energy. A conjectural mechanism, based upon our obtained experimental results, is also presented for photocatalytic applications over Ag/CQDs/ $g\text{-C}_3\text{N}_4$ nanocomposites.

2. Experimental

2.1. Synthesis of carbon quantum dots

CQDs was obtained via alkali-auxiliary sonication method in accordance with the previous literature but modified [18,55]. 9.0 g D-(+)-glucose was uniformly dissolved in 50 mL deionized water, and then 0.8 g sodium hydroxide was added under a constant magnetic stirring. After complete dissolution, the mixed colorless solution was deal with ultrasound for 90 min until the color change to yellowish-brown. Later, the crude product solution was neutralized using HCl to pH = 7, followed by further dialysis treatment with MWCO 1000 dialysis bag for purification. Afterwards, CQDs was dried at 80 °C and stored in aqueous solution with carbon content of 12.504 g/L. Supplementary experiments were carried out in order to study the effect of pH in ultrasonic oscillation on the formation of CQDs by substituting HCl (10 M, 15 mL) or various amounts of NaOH (0 g, 2.0 g) for 0.8 g NaOH.

2.2. Preparation of CQDs/ $g\text{-C}_3\text{N}_4$ nanocomposites

6.0 mL CQDs solution was added into 50 mL ultrapure water containing 10.0 g of urea to form a clear liquid solution through

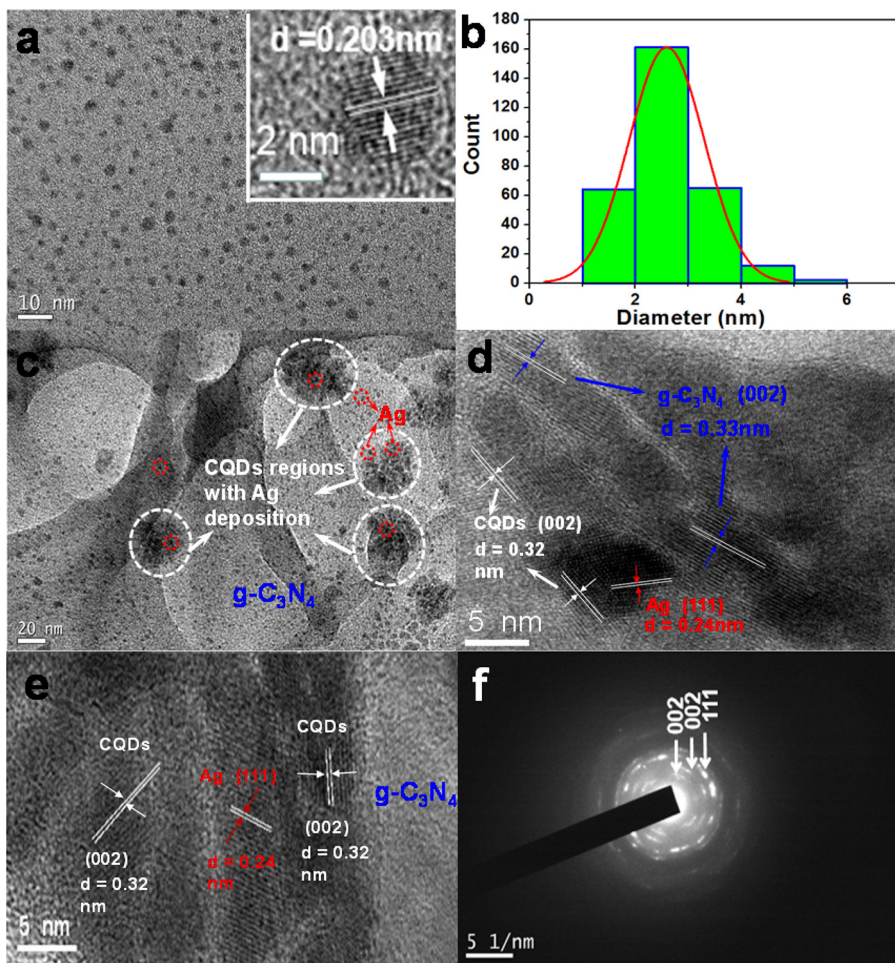


Fig. 1. The TEM image of CQDs obtained with 0.8 g sodium hydroxide in ultrasonication (a), insert: HRTEM of the CQDs; and corresponding particle size distribution of CQDs (b); TEM, HRTEM images (c–e) and SAED pattern (f) of 3 wt% Ag modified 6 mL CQDs/g-C₃N₄ (3S6CCN) nanocomposites.

ultraphonic for 15 min. Then the mixture was dehydrated at 100 °C overnight and heated at 500 °C for 1 h with a heating rate of 5 °C min⁻¹. The obtained conglomeration was ground into powder and collected for further use. Different CQDs content samples, noted as XCCN, were prepared in the same procedure mentioned above except for volume X (mL) of CQDs solution used. The pure g-C₃N₄ was synthesized by heating urea directly in the absence of CQDs.

2.3. Fabrication of Ag/CQDs/g-C₃N₄ photocatalysts

Silver nanoparticles were prepared in terms of the chemical reduction method we reported earlier [6]. Briefly, 8.0 mL of dissolving 8.6 mg PEG 600 aqueous solution was injected into 1.6 mg mL⁻¹ AgNO₃ aqueous solution with the same amount of volume at room temperature. Under vigorous stirring, 9.6 mL deionized water containing 22.5 mg NaBH₄ was poured into the above solution in a fast stream. After continuous stirring for 4 h in an ice-water bath, a certain amount of 6CCN powder was added into the homogeneous suspension by stirring for 20 min and ultraphonic for 1 h. The resulting precipitate was isolated through centrifugation, washed with DI water for three times, and finally dried at 80 °C overnight. In order to investigate the influence of Ag NPs deposition amount on the photocatalytic HER, a series of Ag/CQDs/g-C₃N₄ samples with different mass percentage Y wt% of Ag NPs were exhibited and written as YS6CCN here, where Y is equal to 1, 3, 5, 7 and 9.

For comparison, there is a suite of phtocatalysts designed: (1) Individual Ag NPs were prepared as shown above without any

additive. (2) Ag/g-C₃N₄ composites were synthesized by mixing pure g-C₃N₄ rather than 6CCN. Among them, 3 wt% Ag/g-C₃N₄ (3SCN) composite has been proved earlier to be the best [6]. (3) The Ag/CQDs composites were obtained by mixing CQDs aqueous solution with discrepant volume (2, 4, 6, 8, 10 and 12 mL) and utilizing ultraphonic for 80 min after the Ag NPs were prepared, centrifuged and washed. Then the obtained samples were dried at 80 °C and marked as SXC.

2.4. Characterization

The crystal structure of the photocatalysts was examined on a D8 Advantage X-ray diffraction (XRD) instrument (Bruker, Germany) using Cu-K α radiation ($\lambda = 0.15406$ nm). Fourier transform infrared (FTIR) spectra were detected with a Tensor 27 spectrometer (Bruker) using the KBr flakiness technique. Scanning electron microscopy (SEM) images and energy dispersive X-ray spectroscopy (EDS) were conducted on an Ultra 55 scanning electron microscope. The crystalline morphology and structure informations were acquired from transmission electron microscope (TEM), high-resolution TEM (HR-TEM) and selected area electron diffraction (SAED) images on a JEM-2100HR with an accelerating voltage of 200 kV. X-ray photoelectron spectroscopy (XPS) results were obtained via a Thermo ESCALAB 250Xi spectrometer with a monochromatic Al K α source at 1486.6 eV. Elemental analysis about C, N and O was carried out on a Vario EL cube Elemental Analyzer (Elementar, Germany). The percent content of Ag was

determined by means of inductively coupled plasma atomic emission spectroscopy (ICP-AES). The Brunauer-Emmett-Teller (BET) specific surface area was performed with an ASAP 2020 surface area and porosity analyzer on the basis of N₂ adsorption and desorption isotherms measured at 77 K. UV-vis diffuse reflectance spectra (DRS) were recorded by a Hitachi U-3010 spectrophotometer, with BaSO₄ disk used as reference standard. Photoluminescence (PL) character of the samples was studied on an F-4500 fluorescence spectrograph. Raman spectra were captured by dint of a Micro Raman spectrometer (LabRAM Aramis, H.J.Y) utilizing a 1200 g mm⁻¹ grating and a 632.8 nm He-Ne laser source for excitation.

2.5. Photocatalytic hydrogen generation performance

The photocatalytic measures were conducted in virtue of an external 300 W xenon lamp (PLS-SXE300) fitted with matching cut-off filter (550 nm) or band-pass filters (400 ± 20, 700 ± 20, 800 ± 20 and 900 ± 20 nm) and a 300 mL outer-irradiation Pyrex vessel, which was equipped with a closable gas circulation connected to a vacuum air-removed system for thorough degassing. Typically, 5 mg target photocatalyst was dispersed in a 70 mL water solution containing 10 mL triethanolamine as the sacrificial agent by magnetic stirring. A persistent stirring and circulating cooling water were necessities in the whole reaction to guarantee the suspension homogeneity at normal temperature. The specific H₂ release amount was evaluated by online GC7900 gas chromatography (5 Å molecular sieve column, TCD detector) with high purity N₂ as carrier gas. Subsequently, triethanolamine was replaced by triethylamine (TEA), N, N-Dimethylformamide (DMF), ethylene glycol (EG), ascorbic acid (AA) and lactic acid (LA), which all possess the same molar quantity, to decide the optimal sacrificial agent for this system.

The apparent quantum efficiency (AQE) was determined in the same testing environment except for demanding a bandpass filter to afford a monochromatic incident light at $\lambda = 400 \pm 20$ nm, which was 12 cm away from the liquid surface. The mean intensity of the light source was calculated to be 16.38 mW cm⁻² and the irradiated area was 50.24 cm². The QE results were estimated as the following formula (Eq. (1)):

$$QE = \frac{\text{The number of captured electrons}}{\text{The number of incident photons}} \times 100\% \quad (1)$$

$$= \frac{\text{The total number of released H atoms}}{\text{The number of incident photons}} \times 100\%$$

2.6. Electrochemical measures

The photocurrent tests and electrochemical impedance spectra (EIS) were operated on an electrochemical workstation (CHI660C, China) in a traditional three-electrode cell with 0.1 M NaSO₄ aqueous solution as electrolyte. A Pt coil was employed as the counter electrode and Ag/AgCl electrode served as the reference electrode. Pure g-C₃N₄, 6CCN and 3S6CCN electrodes as working electrodes were made imitating the records [64]. The photocurrents were measured at 0.0 V with the 300 W Xe-lamp on and off. EIS curves were recorded under the open circuit voltage in the frequency range of 10²–10⁶ Hz with an ac amplitude of 10 mV.

3. Results and discussions

3.1. Morphology

Fig. 1a displays the TEM image of as-prepared carbon quantum dots obtained from glucose by ultrasonic waves with 0.8 g of NaOH.

As can be seen, they are monodispersed quasi-spherical particles with an average diameter of ca. 2.59 nm and mainly distributed in 1–5 nm by counting 304 nanoparticles (Fig. 1b). HRTEM image of the crystalline regions shows an interplanar spacing of 0.203 nm, which conforms to (1 0 1) lattice plane from graphitic carbon [59]. It is interesting to aware that pH of the reaction solution has an obvious impact on the formation of CQDs. As shown as Fig. S1, for utilizing glucose as the reactant in the absence of NaOH or in the presence of HCl, there are no any variance in color observed after ultrasonic processing, demonstrating it is hard to form CQDs in such conditions. Upon the addition of more NaOH, solution color gets a darker brown, suggesting a new substance has been produced, nevertheless, the product shows a tendency of agglomeration and the particles contact with each other closely to cause lattice overlapping (Fig. S2). The generating mechanism of CQDs has been proposed previously [55]. In the reaction system, OH⁻ primarily acts as a catalyst to induce the formation of CQDs [47]. Furthermore, OH⁻ may affect the surface states of CQDs and excessive OH⁻ are detrimental to decentralization of generated radicals, which should result in aggregate C-dots due to instant crosslinking between the crowded radicals. Morphology of as-produced 3S6CCN was characterized by TEM (Fig. 1c), showing that CQDs were more inclined to distribute nonuniformly, with obvious regions of dense dark spots embedded in the nanosheets of g-C₃N₄, and silver nanoparticles lay scattered on carbon dots regions in addition to the surface or interlayer of g-C₃N₄ randomly. During the sonication process, some g-C₃N₄ nanoplates were partially deposited on the Ag NPs under the effect of coordination between unoccupied orbital of Ag and the lone pair electrons of N in the nitrogen pots of g-C₃N₄ framework, along with the development of coherent interface and Schottky barrier, so the Ag NPs intercalated the interlayer of g-C₃N₄ to form a heterojunction structure steadily [65–67]. The size of the Ag NPs has been calculated to be mainly 2–5 nm with mean diameter about 3.45 nm before in the same synthetic method [6]. HRTEM images (Fig. 1d and e) was collected to further illustrate the formation of Ag/CQDs/g-C₃N₄ complex. At the higher magnification, the lattice fringes with $d = 0.33$ nm is consistent with (0 0 2) facet of g-C₃N₄ [10]. Alongside g-C₃N₄ crystallines, as can be easily found, the lattice spacing of 0.32 nm corresponding to (0 0 2) plane of graphitic-like carbon [58] and the lattice spacing of 0.24 nm matching (1 1 1) spacing of metallic Ag [6], which sit intimately and overlap with each other, provide persuasive evidence for the formation of heterostructures, promoting the photoelectrons migrate in the heterogeneous interface smoothly. Unlike primordial CQDs, a lattice variation of CQDs in hybrid Ag/CQDs/g-C₃N₄ nanocomposites happened through calcination treatment, owing to the transformation of hexagonal graphite crystallization to turbostratic structure [45]. The SAED pattern (Fig. 1f) revealed the crystalline nature of 3S6CCN with bright diffraction rings accorded with (0 0 2) plane of g-C₃N₄, (0 0 2) plane of graphitic carbon and (1 1 1) plane of Ag nanoparticles, successively.

Fig. 2 compares the exterior configuration of pristine and modified g-C₃N₄ photocatalysts. Primarily, pure g-C₃N₄ embodies porous laminar microstructure consistently as presented in Fig. 2a. Fig. 2b shows that spatial density increased whether on the surface or in pores of g-C₃N₄, following by new pores taking shape, as carbon quantum dots were introduced into g-C₃N₄ matrix. And, Ag/CQDs/g-C₃N₄ composites present more compact and rough surfaces (Fig. 2c and d), implying nanoscale silver has deposited on 6CCN. As can be seen in Fig. 2d, some thinner lamellas of g-C₃N₄ also were severed when the modification of Ag to be 3%. As illustrated above, the heterojunctions between Ag, CQDs and g-C₃N₄ have developed and should be conducive to effective separation of photoelectrons from vacancies. Nevertheless, when Ag content at extravagant levels over 5% (Fig. 2e–g), the agglomerate phenomena will occur and the massive chunks will act as new recombination

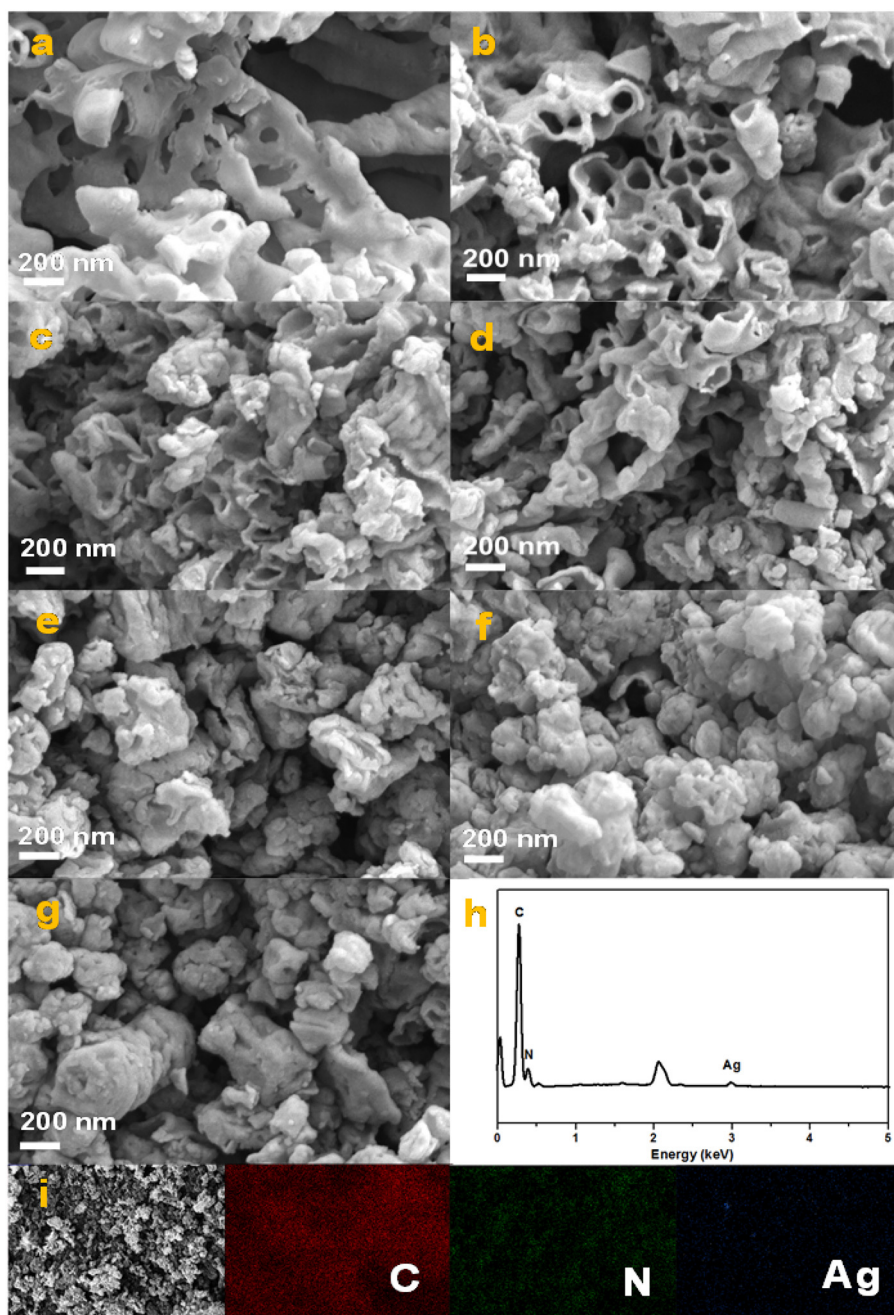


Fig. 2. SEM images of as-prepared pristine $\text{g-C}_3\text{N}_4$ (a), CQDs/ $\text{g-C}_3\text{N}_4$ (6CCN) (b), Ag/CQDs/ $\text{g-C}_3\text{N}_4$ samples of 1S6CCN (c), 3S6CCN (d), 5S6CCN (e), 7S6CCN (f) and 9S6CCN (g), respectively; the EDS spectrum (h) and elemental mapping patterns (i) of 3S6CCN.

Table 1

S_{BET} pore volume, average pore size, H_2 evolution rate (HER) and AQE of the as-prepared photocatalysts.

Sample	S_{BET} ($\text{m}^2 \text{g}^{-1}$)	Pore volume ($\text{cm}^3 \text{g}^{-1}$)	Average pore size (nm)	H_2^{a} ($\mu\text{mol h}^{-1} \text{g}^{-1}$)	AQE ^b (%)
$\text{g-C}_3\text{N}_4$	29.6	0.027	3.6	94.23	0.84
6CCN	29.5	0.031	4.2	220.77	2.08
3S6CCN	25.4	0.035	5.4	344.51	3.50
3S6CCN	34.4	0.072	8.4	626.93	4.81

^a Reactions were carried out under a 300 W Xe-lamp.

^b AQE was estimated based on the amount of hydrogen production under a monochromatic light irradiation ($\lambda = 400 \text{ nm}$) for 2 h with 0.06 g photocatalysts.

centers, debasing photocatalysts activity and apparent quantum yield. EDS and elemental mapping spectra (Fig. 2h and i) also were performed to confirm the existence of C, N and Ag elementals in 3S6CCN specimen after eliminating the extra inevitable elementals.

3.2. Structural characterization and composition

XRD patterns were utilized to provide further support for identifying and determining the different phase structures of the

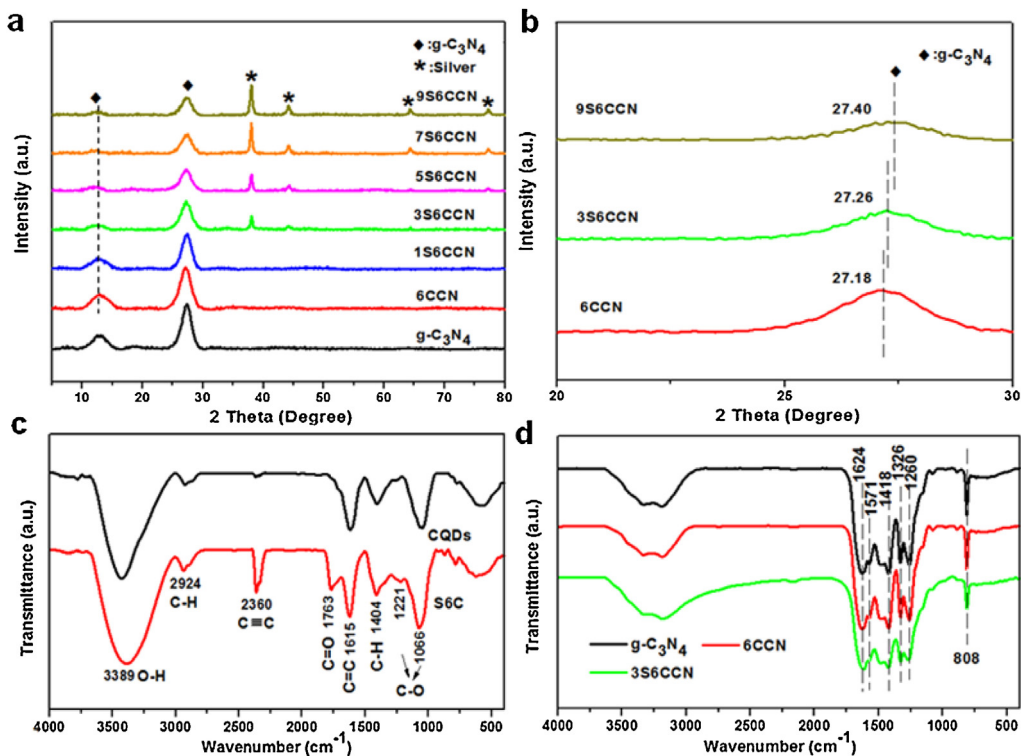


Fig. 3. XRD patterns of the pure g-C₃N₄, CQDs/g-C₃N₄ (6CCN) sample and Ag/CQDs/g-C₃N₄ composites with different doping amounts of Ag (a), together with the magnified parts of 6CCN, 3S6CCN and 9S6CCN sample (b); FTIR spectra of the CQDs and Ag/CQDs (S6C) (c), pure g-C₃N₄, CQDs/g-C₃N₄ (6CCN) and Ag/CQDs/g-C₃N₄ (3S6CCN) (d).

synthesized samples. As we can see, pristine g-C₃N₄ possesses two obvious diffraction apices, which agree with the result in the literature [68]. The sharper one at 27.4° indexed as (0 0 2) diffraction peak with an interlayer distance of about 0.34 nm represents interlayer-stacking structure of conjugated aromatic system. While the weaker one at 13.0° derived from the inter-planar structural packing is indexed as (1 0 0) diffraction plane, conforming to a distance of 0.68 nm [60,69]. As shown in Fig. S3a, as the usage amount of CQDs changed from 2 mL to 12 mL, the phase structure of g-C₃N₄ can still be retained well in general, but only a slight motion happened on the (0 0 2) diffraction peak toward the lower angle value gradually from 27.35° to 27.07° (Fig. S3b), which is ascribed to the intense interaction between g-C₃N₄ and CQDs that result in the formation of defects and lattice distance augment [56,60]. However, the characteristic peaks of graphite carbon could not be observed here, perhaps this is because of the low dosage of CQDs or amorphous carbon in a significant portion. When loading mass of Ag NPs was increased from 3% to 9% (Fig. 3a), the intensity of the diffraction peaks assigned to Ag as JCPDS no. 089-3722 heightened gradually, along with the diffraction intensity of two characteristic peaks from g-C₃N₄ accordingly reduced. This suggests that the introduction of Ag would exfoliate the nanolayers of g-C₃N₄ and influence its stacking structure by SPR effect [65]. Furthermore, it is interesting to note that (0 0 2) peak relative to g-C₃N₄ slightly shifts from 27.18° to 27.40° with increasing of silver, which means that the interlayer distance then decreased after modification of Ag NPs based on 6CCN. This may be because interlayer Ag adjusted the distance of layers, suggesting the Ag NPs were not limited to the shallow surface [70–72]. The primary particle size of Ag for all samples ranges from ca. 14 to 23 nm related to the silver increase (Table S1), as obtained from Scherrer analysis of the corresponding XRD patterns. It is noted that the averaged size values from XRD is bigger than that calculated from TEM since the latter gives a partial particle size distributions [73]. Fig. S3d indicates that crystalline

structure of Ag NPs keeps well with the existence of CQDs in S6C sample.

Fig. 3c and d described the FTIR spectrograms of bare CQDs, g-C₃N₄ and related compound photocatalysts. Contraposing pure CQDs and S6C, the characteristic peaks belong to functional groups of CQDs were observed over both of them. The broad peak at 3389 cm⁻¹ is due to stretching vibration of O–H. The peaks at 2924 cm⁻¹ and 1404 cm⁻¹ corresponds to the stretching vibration and bending vibration of C–H [47]. Furthermore, the characteristic absorption at 2360 cm⁻¹ and 1625 cm⁻¹ are related to the stretching modes of C≡C and C=C respectively, which contributes to the photoluminescence of CQDs due to π–π* transition [45]. The band at 1763 cm⁻¹ for C=O stretching vibration, combined with the peaks derived from C–O (C–O–C and C–O–H) stretching modes at 1221 and 1066 cm⁻¹, demonstrate the presence of surface groups such as hydroxyl, carboxyl and carbonyl on CQDs [48]. For bare g-C₃N₄, CQDs/g-C₃N₄ and Ag/CQDs/g-C₃N₄ complex (Figs. 3c and S3c), several major vibrations in the range of 1260 cm⁻¹ to 1624 cm⁻¹ represents the typical stretching peaks of CN heterocycle structure. In addition, the particular breathing mode for triazine rings of g-C₃N₄ appears at 808 cm⁻¹ and the broad absorption centered at around 3280 cm⁻¹ corresponds to the N–H vibration of uncondensed amino groups [6,71]. Whereas, the characteristic peaks about CQDs are hardly found in all the g-C₃N₄-related photocatalysts as the reports in literatures [59–61], signifying the low doping levels of CQDs here, as well as Ag NPs, did not damage the integral structure of g-C₃N₄ as the host.

In order to acquire profound comprehension on the interactions, XPS technique was further performed to confirm the specific surface composition and elemental status (Fig. 4). The survey spectrum of the 3S6CCN sample is shown as Fig. 4a, indicating the hybrid is mainly composed of C, N, O and Ag elements. The accurate mass percentage ratio of C: N: O: Ag was evaluated as 31.60: 54.35: 8.26: 2.94 with the assist of elemental analyzer and ICP-AES apparatus. Fig. 4b displays the high-resolution XPS in the C 1 s binding energy

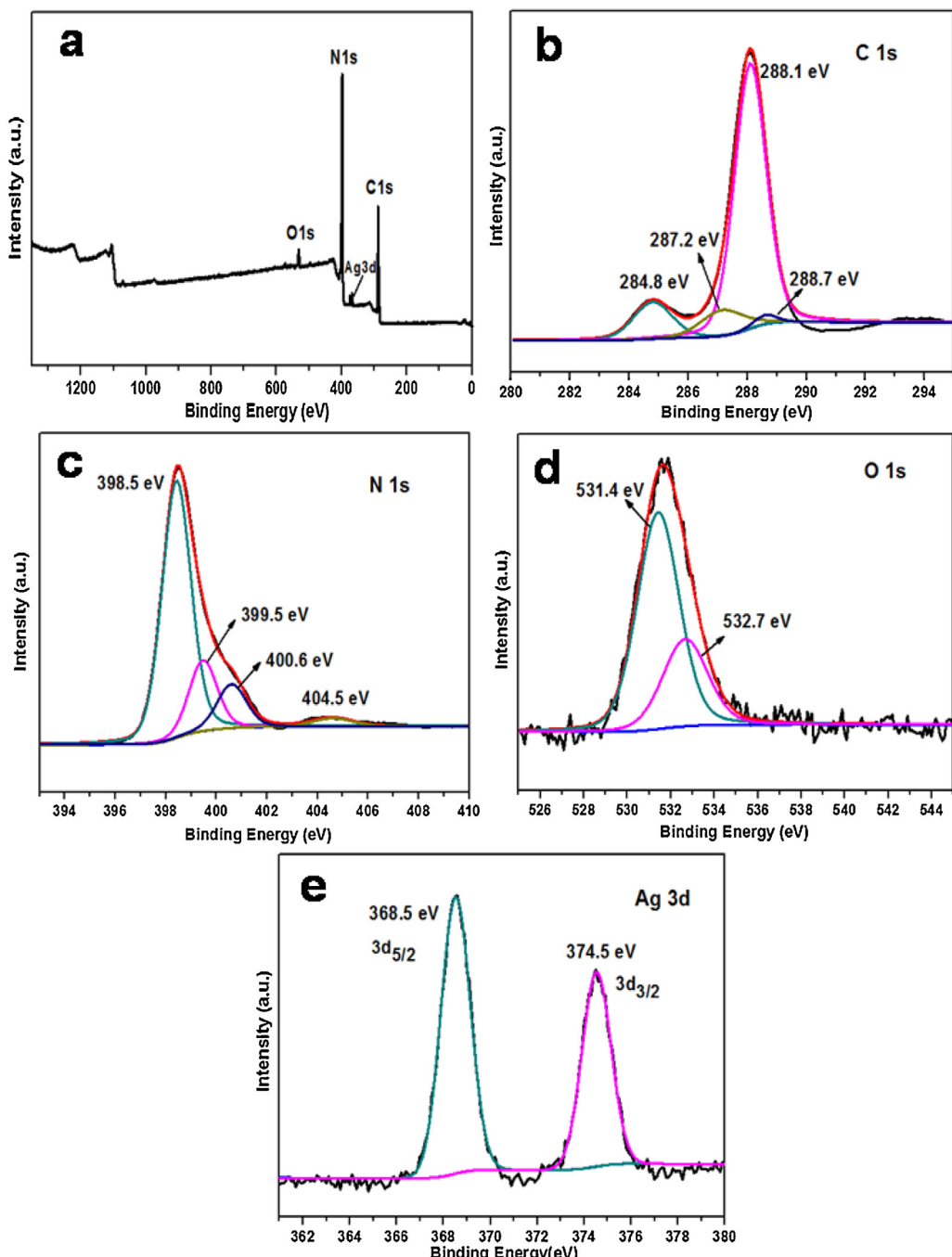


Fig. 4. XPS spectra of the as-synthesized 3S6CCN (3 wt% Ag/6 mL CQDs/g-C₃N₄) composite.

regions, and the typical spectrum has been fitted into four peaks at 284.8, 287.2, 288.1 and 288.7 eV, which can be assigned to C—C/C=C bonds, C—O bonds, sp²-hybridized atomic carbon in N—C=N and carboxyl-C in O=C—O, respectively [5,10,45,71]. Besides, the XPS spectrum of N 1s (Fig. 4c) from the g-C₃N₄ has been deconvoluted into four species: sp²-bonded N (C=N=C) in triazine rings at 398.5 eV, tertiary N in N-(C)₃ at 399.5 eV, amino groups (N—H) at 400.6 eV, and the remaining one centered at 404.5 eV is ascribable to the π excitations [59,73]. As shown in the O 1s core level spectrum (Fig. 4d), the major peak centered at 531.4 eV corresponds to O—C/O—H bonds, while the binding energy at 532.7 eV belong to O=C [9], which both can be ascribed to the oxygenic components of CQDs. The strong shaken-up satellite doublet of Ag 3d with binding energies of 368.5 eV and 374.5 eV are identified as Ag 3d_{5/2}

and Ag 3d_{3/2} orbitals attributed to metallic Ag [47,63]. The results shown in Table S2 exhibit the slight shift of the different peaks of C- and N-containing chemical components in the photocatalysts with respect to g-C₃N₄-based systems, so the introduction of silver and CQDs has little influence on the chemical modification of g-C₃N₄ parent.

In consideration of the different physical textural properties, Table 1 has displayed BET specific surface area, pore volume and average pore size of the samples. Among them, we have reported all values of g-C₃N₄ and 3SCN (3 wt% Ag/g-C₃N₄) before [6]. Compared with bulk g-C₃N₄, the 6 mL CQDs/g-C₃N₄ (6CCN) sample exhibits very similar S_{BET} and larger pore volume, average pore diameter, which means that calcining the mixture of CQDs and g-C₃N₄ does not change the specific surface area more, but causes the slight

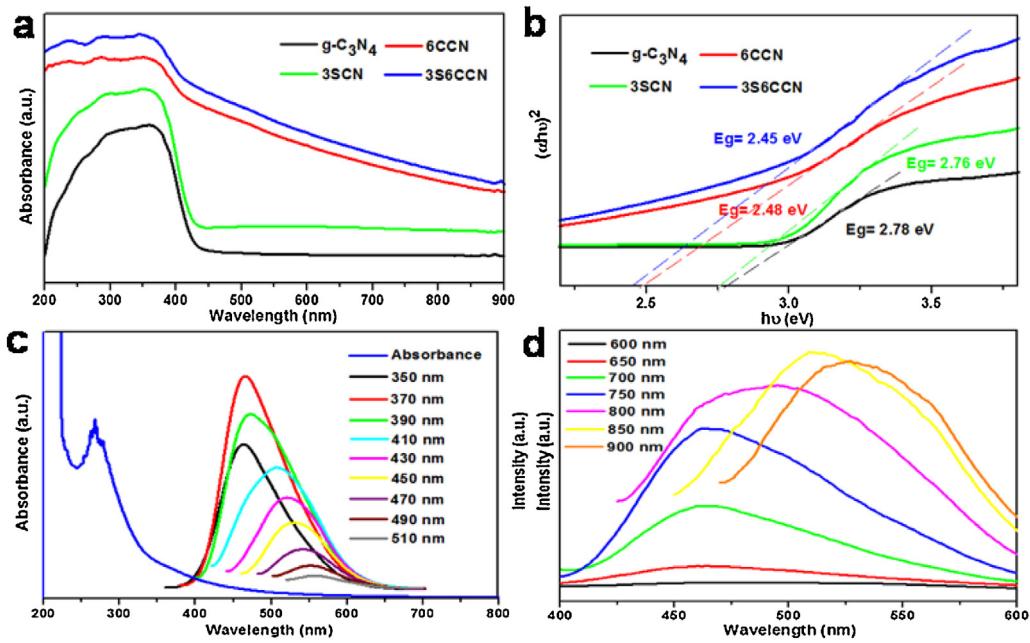


Fig. 5. UV-vis DRS (a) and $(\alpha h\nu)^2$ versus $h\nu$ curve (b) of $\text{g-C}_3\text{N}_4$, CQDs/ $\text{g-C}_3\text{N}_4$ (6CCN), Ag/ $\text{g-C}_3\text{N}_4$ (3SCN) and Ag/CQDs/ $\text{g-C}_3\text{N}_4$ (3S6CCN); UV-vis absorption and down-converted photoluminescence (c), up-converted photoluminescence spectra (d) of synthetic CQDs.

expansion of the pores. Coincidentally, with proper loading amount of Ag NPs embedded in the interlayer of $\text{g-C}_3\text{N}_4$ (shown in Fig. S4), the nanosheets of 3SCN were skived and a number of new pores were formed [6], leading to the smaller S_{BET} but larger pore volume and average size. Just because of this, both 6CCN and 3SCN exhibited their own a bit of superiority on photocatalytic H_2 evolution and apparent quantum efficiency. What is more, introducing Ag NPs into the CQDs/ $\text{g-C}_3\text{N}_4$ nanocomposite will incur the more pronounced surface area and mesoporous dimensions as shown as 3S6CCN (3 wt% Ag/6 mL CQDs/ $\text{g-C}_3\text{N}_4$), which may result from the in-depth shaving even severing of the thinner nanolayer on 6CCN, generating more pores to expose. It is noted that other Ag/CQDs/ $\text{g-C}_3\text{N}_4$ photocatalysts are also no match for 3S6CCN in surface area and mesostructure (Table S1), because the less Ag NPs (1%) may block the mesopores and the more (5–9%) have the tendency to aggregate. The proper specific surface area and mesoporous architecture contribute to more active sites for molecular absorption of reactants and transportation of products. Hence, 3S6CCN possesses the highest photocatalytic H_2 generation activity and apparent quantum efficiency in all of the samples.

3.3. Optical properties

The optical properties of the obtained all kinds of samples were investigated by UV-vis DRS, PL and Raman spectra at room temperature. As we can see in Fig. 5a, the pristine $\text{g-C}_3\text{N}_4$ has an innate absorption limit at around 460 nm, while Ag/ $\text{g-C}_3\text{N}_4$ samples show an additional visible-light absorption peak in the region from 410 to 550 nm (Fig. S5) due to intense surface plasmon resonance of nanostructured silver [44,73]. It is amazing to notice that clear red shift appears both on the optical absorption edge of 6CCN and 3S6CCN with less degenerative light capture tailing out to (near) IR region, elucidating the effective combination of CQDs with other components. Due to the presence of surface plasmon resonance from nanosilver particles, 3S6CCN nanocomposite exhibited higher absorption intensity on the basis of 6CCN, which in turn proves the successful loading of Ag NPs. Additionally, Fig. S6 shows that light harvesting capacity of CQDs/ $\text{g-C}_3\text{N}_4$ and Ag/CQDs/ $\text{g-C}_3\text{N}_4$ heterostructures increases gradually as increasing CQDs and Ag

amount, respectively. The corresponding direct band gaps of semiconductors (Fig. 5b) are determined by converted $(\alpha h\nu)^2$ versus $h\nu$, where α , h and ν represents absorption coefficient, Planck constant and optical frequency, respectively [44,59]. Band gaps of the composites drastically narrow with the modification of CQDs and E_g value of 3S6CCN has shrunk from 2.78 eV to 2.45 eV, which may be suitable for absorbing more visible light even near-infrared light to improve the H_2 evolution and apparent quantum yield. Apart from the reduced band gap, the valence band energy (E_{VB}) of 3S6CCN is estimated to be 1.49 eV by valence band X-ray photoelectron spectroscopy (VBXPS) in Fig. S7. Therefore, the conduction band position is calculated to be -0.96 eV, which is matching for H^+ reduction to H_2 . In conclusion, this Ag/CQDs/ $\text{g-C}_3\text{N}_4$ hybrid system has presented its great potential to become a practical photocatalytic material.

In order to elaborate more details for promising superiority of CQDs in the photocatalysts, down-conversion and up-conversion photoluminescence (PL) properties were explored by varying different excitation wavelengths (Fig. 5c and d). As shown in Fig. 5c, a characteristic UV-vis absorption peak of CQDs solution emerges at ~ 270 nm, attributed to the $\pi-\pi^*$ and $n-\pi^*$ transition of nanocarbon particles [48,58]. The PL emission spectra of solution exhibited excitation wavelength-dependent fluorescence behavior. As the excitation wavelength ranging in 350–510 nm, the emission peaks were shifted from 460 nm (black) to 560 nm (gray), along with intensity decreasing gradually. This phenomenon can be interpreted as the radiative recombination of surface trapping states, which initiates multiple or different emission sites at various excitation wavelengths [51,58,74]. And when excited at 370 nm, the maximum emission of CQDs appears at 465 nm with a full-width at half maximum (FWHM) about 85 nm. Smaller FWHM, to the best of knowledge, can be used as the indication of narrower size distribution [48], and the obtained FWHM in here signifies narrower particle size distribution of the as-prepared CQDs, in accordance with the TEM results. Above all, CQDs continues to display up-converted PL property (Fig. 5d), which can absorb longer-wavelength light in visible (600, 650, 700 nm) and NIR (700, 800, 900 nm) region and then emit visible light with shorter wavelength located at 400–550 nm, that in turn excite the

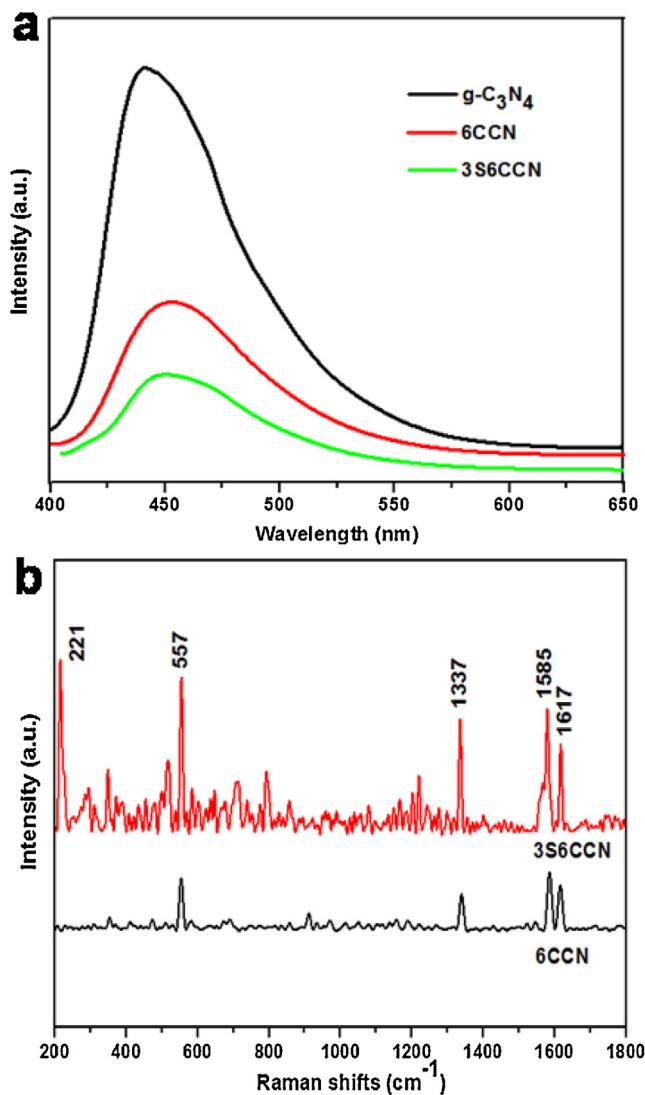


Fig. 6. PL spectra (370 nm excitation) of $\text{g-C}_3\text{N}_4$, CQDs/ $\text{g-C}_3\text{N}_4$ (6CCN) and Ag/CQDs/ $\text{g-C}_3\text{N}_4$ (3S6CCN) (a); Raman spectra of 6CCN and 3S6CCN (b).

visible-light photocatalysts to generate photo-induced electron-hole pairs, demonstrating CQDs can serve as a photosensitizer to make Ag/ $\text{g-C}_3\text{N}_4$ components effectively harness visible light with wavelengths above 550 nm to realize broad spectrum utilization and improve the photocatalytic performance. Such fascinating property should be ascribed to multiphoton active process [71,74]. Meanwhile, the surface plasmonic oscillation of Ag NPs can further strengthen the light-harvesting capability of CQDs.

As we all know, CQDs have been confirmed excellent as both electron donors and electron acceptors [44,62]. In subsequent experiments, the migration and separation circumstance of photo-generated electron-hole pairs were investigated by PL spectra. In Fig. 6a, the similar broad emission band centered at 440–455 nm appears on all the samples with excitation wavelength set at 370 nm. As can be clearly seen, compared with the highest PL peak of pure $\text{g-C}_3\text{N}_4$, emission intensity for 6CCN substantially decreases, indicating the recombination of photo-induced electrons-holes is efficiently suppressed after appropriate amount of CQDs modification. Moreover, the intensity for 3S6CCN is comparatively lower than the former two, which demonstrates the photoelectrons were ulteriorly transferred *via* interface to accelerate the carrier separation by Ag NPs modified. This is why Ag/CQDs/ $\text{g-C}_3\text{N}_4$ hybrid shows the supreme photocatalytic capacity and apparent quantum efficiency.

The effective quenching of CQDs' PL intensity in Ag/CQDs system (Fig. S9) and existence of plasmon-induced resonance energy transfer (RET) from noble metals guarantee the mutual ultrafast electron transfer between Ag particles and CQDs [49].

Fig. 6b shows Raman spectra of 6CCN and 3S6CCN samples. There are four characteristic peaks detected on 6CCN, and two representative D-band and G-band peaks assigned to CQDs were observed at 1337 and 1617 cm^{-1} respectively. The D-band belongs to vibrations of C atoms with dangling bonds in the planar terminals of disordered graphite, while the G-band corresponds to the ordered graphite structures [44,56,62]. The remaining two peaks located at 557 and 1585 cm^{-1} are attributed to $\text{g-C}_3\text{N}_4$, one at 557 cm^{-1} is derived from symmetric stretching vibration state of heptazine heterocycles, and the other band at 1585 cm^{-1} , defined as G band, is associated with C=N stretching vibration, which confirms the formation of graphite-like structures [6]. In comparison with 6CCN, Raman intensity of the above four features is enhanced in Ag/CQDs/ $\text{g-C}_3\text{N}_4$ nanocomposites due to the presence of surface enhanced Raman scattering (SERS) effect from Ag NPs with suitable shapes and sizes. Moreover, the latter observation exhibits a new Raman peak at 221 cm^{-1} , in consonance with Ag-N symmetric vibration mode [6]. Considering these results, we can conclude that a close-knit interaction exists in the three components to accelerate photo-induced electrons transfer.

3.4. Photocatalytic H_2 generation and stability tests

The photocatalytic hydrogen production activity of all the catalysts was assessed under a 300 W Xe-lamp without any optical filter, which resembles solar light irradiation. As can be seen in Fig. 7a, the novel assembly system, Ag/CQDs/ $\text{g-C}_3\text{N}_4$, has shown significantly enhanced photocatalytic ability with evidently higher HER in contrast to alone $\text{g-C}_3\text{N}_4$ with the lowest hydrogen evolution as 94.23 $\mu\text{mol g}^{-1} \text{h}^{-1}$. The photocatalytic HER of the composites increases at first and then decreases gradually with the growth in introduced Ag NPs amount. Among the ternary systems, 3S6CCN shows the maximum photocatalytic H_2 generation datum of 626.93 $\mu\text{mol g}^{-1} \text{h}^{-1}$, which is about 6.7 times higher than that of pure $\text{g-C}_3\text{N}_4$. However, once the content of Ag particles exceeds 3 wt% to reach 5, 7 or 9 wt%, a distinct decline of photocatalytic activity will appear owing to the superfluous accumulation of Ag NPs, shielding active reaction sites and restraining the suppression of carriers recombination [64], that could be more intuitively obtained in aforementioned SEM and BET results. Prior to the construction of Ag/CQDs/ $\text{g-C}_3\text{N}_4$ heterostructures, the optimal specimen from every series of binary systems has been singled out for contrast, as 3SCN obtained in our recent work [6], 6CCN and S6C shown in Fig. S10. It is noted that the photocatalytic capability of twain is superior to the pristine one in Fig. 7b. This is because, from the known results, whether bearing right amount of Ag NPs or CQDs both contribute to a better visible-light acquisition and division of electron-hole pairs. It is worth mentioning that S6C system with minor particle size (Fig. S11) also shows a considerable photocatalytic HER (208.47 $\mu\text{mol g}^{-1} \text{h}^{-1}$), may ascribed to RET process between CQDs and Ag NPs, which is mentioned here for photocatalytic hydrogen production for the first time. Sequentially, photocatalytic performance of ternary Ag/CQDs/ $\text{g-C}_3\text{N}_4$ heterostructures further soars to 626.93 $\mu\text{mol g}^{-1} \text{h}^{-1}$ on the foundation of 6CCN, increased by a factor of ca. 2.8 in the presence of Ag NPs, indicating Ag particles would further facilitate the light absorption and transfer of photoelectrons by utilizing its own strong plasmonic effect. In order to explore the influence of sacrificial-agents choice on hydrogen generation, various classes of reagents with coincident molar concentration were adopted to reduce photo-generated holes. As shown in Fig. 7c, alcohol and acid materials to which ethylene glycol (EG), ascorbic acid (AA) and lac-

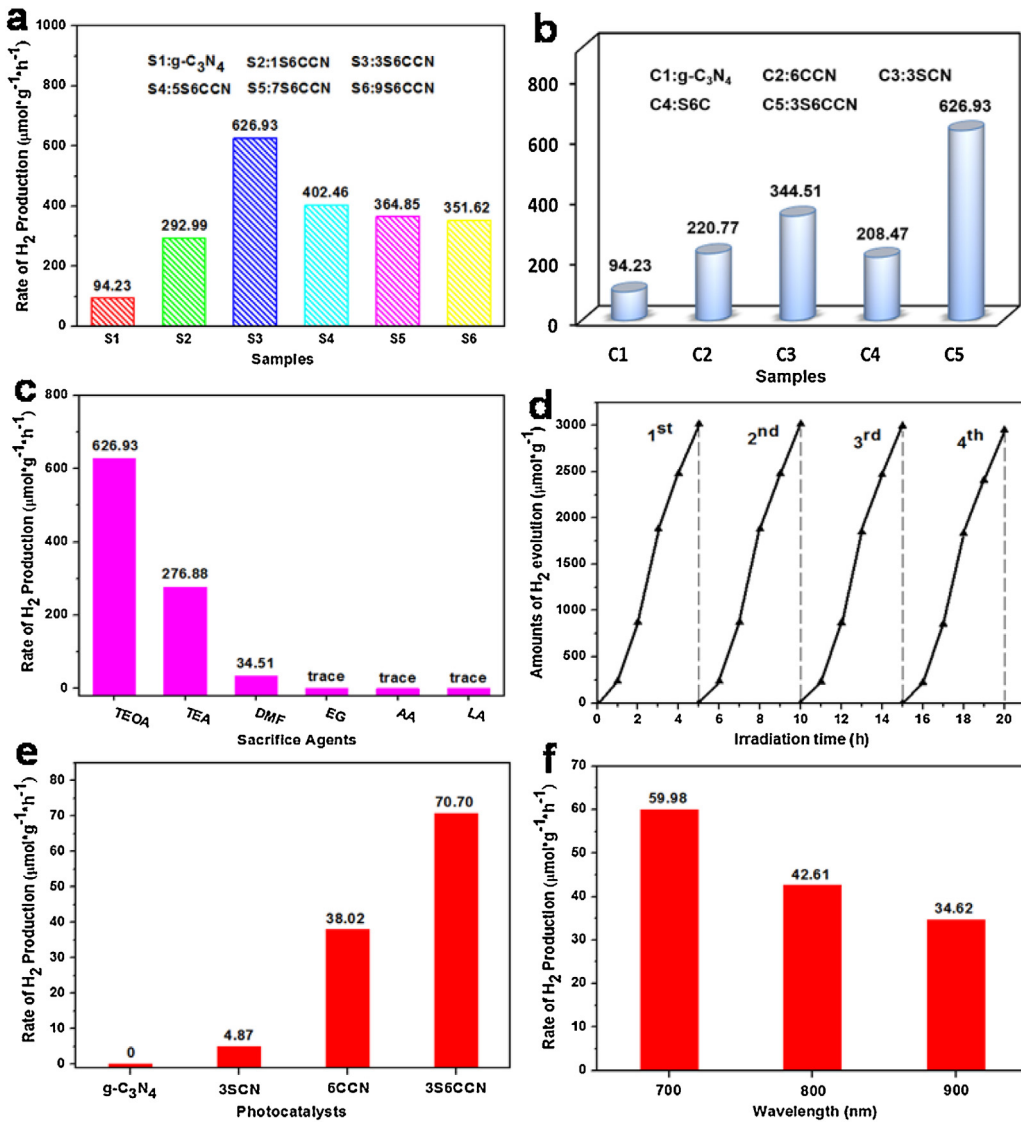


Fig. 7. Photocatalytic activity of the investigated photocatalysts (0.005 g) in an aqueous solution (70 mL) containing TEOA (10 mL) as the sacrificial agent: H₂ evolution rates (HER) of pure g-C₃N₄ and Ag NPs modified 6CCN (6 mL CQDs/g-C₃N₄) composites with different contents (a), the optimal samples of unary (g-C₃N₄), binary (CQDs/g-C₃N₄, Ag/g-C₃N₄, Ag/CQDs) and ternary (Ag/CQDs/g-C₃N₄) (b), and 3S6CCN (3 wt% Ag/6 mL CQDs/g-C₃N₄) with different kinds of sacrificial agents (c) under visible light similar to solar light irradiation (illumination time = 3 h); recycling performance of 3S6CCN towards photocatalytic H₂ generation (illumination time = 20 h) (d); HER of g-C₃N₄, 3SCN (3 wt% Ag/g-C₃N₄), 6CCN and 3S6CCN under long wavelength ($\lambda > 550$ nm) irradiation (e), and HER of 3S6CCN upon NIR monochromatic light with $\lambda = 700$ nm, 800 nm or 900 nm (f) (illumination time = 3 h).

tic acid (LA) belong, have no effect on the whole photocatalytic process with feeble hydrogen detection signal, which is analogous to the situation that no sacrificial-agents existed. However, H₂ evolution was detected when the sacrificial-agents were replaced by common amine substances, such as N, N-Dimethylformamide (DMF), triethylamine (TEA) and triethanolamine (TEOA). This result may be interpreted as that lone pair electrons of nitrogen atoms in amine were more prone to interacting with holes. For that matter, electron-donating ability sequence of nitrogen atoms is TEA > TEOA > DMF, additionally, the boiling point of TEA is so low (89.5 °C) that it was evaporated easily during vacuumization and illumination treatment. Hence, DMF just shows a little effect on hydrogen generation, and yet TEOA is the optimized sacrificial agent to consume photo-generated holes of g-C₃N₄, guaranteeing that more photoelectrons were released to combine with H⁺ for hydrogen evolution.

For practical applications, the stability of Ag/CQDs/g-C₃N₄ photocatalysts was investigated by repetitive time-circle photo-

catalytic hydrogen generation for consecutive four cycles (20 h) over 3S6CCN as the representative nanocomposite (Fig. 7d). Incipiently, the hydrogen generation efficiency gradually increased as time in the first three hours during each repetition, and then began to obviously decrease in the fourth hour, due to the oxidation and consumption of TEOA as electron donors. There is no distinguishable discrepancy observed in catalytic effect after four periods under visible light illumination, suggesting the splendid stability and reusability of as-prepared heterostructure with the prolonged reaction duration [56]. Moreover, PXRD patterns and FTIR spectra of 3SCCN before and after the circulation test remained fairly consistent (Fig. S12), and thus validating the photostability and thermostability of the photocatalyst.

To better verify and elucidate the broad spectral absorption properties of Ag/CQDs/g-C₃N₄ heterostructures, photocatalytic control-experiments of a variety of correlative photocatalysts were designed under long wavelengths irradiation using a 550 nm cut-off filter (Fig. 7e). As is well known, g-C₃N₄ and Ag/g-C₃N₄ compos-

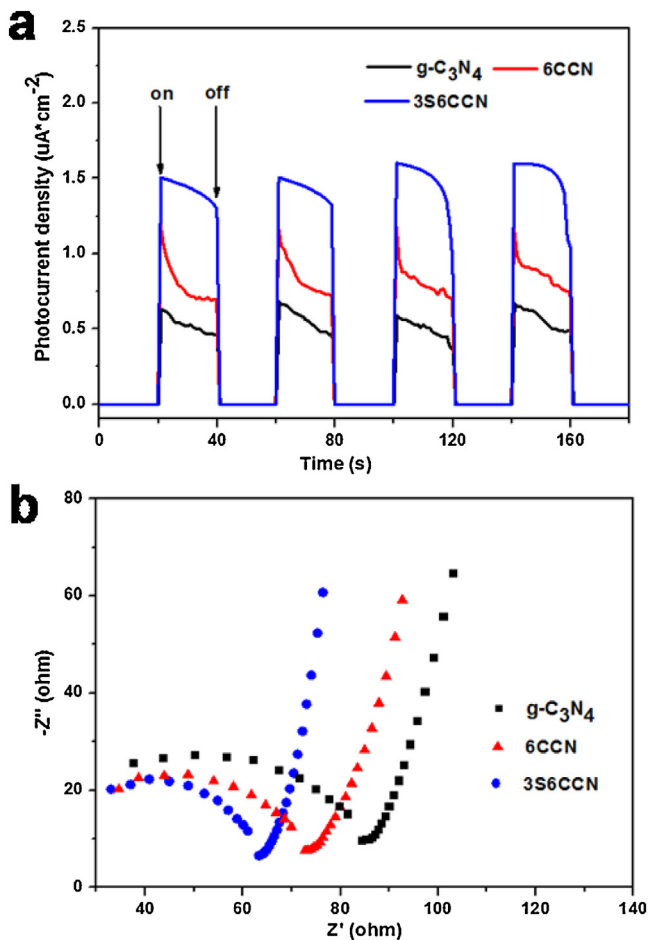


Fig. 8. Transient photocurrent responses of pure $\text{g-C}_3\text{N}_4$, CQDs/ $\text{g-C}_3\text{N}_4$ (6CCN) and Ag/CQDs/ $\text{g-C}_3\text{N}_4$ (3S6CCN) under 300 W Xe-lamp irradiation without cutoff filters for four on-off cycles (a); EIS Nyquist plots of pure $\text{g-C}_3\text{N}_4$, 6CCN and 3S6CCN (b).

ites lack the absorption of visible light with wavelengths beyond 550 nm (Fig. 5a). Notably, pure $\text{g-C}_3\text{N}_4$ and 3SCN displayed no or weak ($4.87 \mu\text{mol g}^{-1} \text{h}^{-1}$) hydrogen evolution signal, while 38.02 and $70.70 \mu\text{mol g}^{-1} \text{h}^{-1}$ were detected on 6CCN and 3S6CCN, respectively. These results once again corroborate the samples, which comprises the CQDs, can take advantage of long wavelengths to emit short wavelengths, attributed to the upconversion property of CQDs. Especially, in such situation, the HER of 3S6CCN still exceeds that of 6CCN, which should be caused by the surface plasmon resonance effect of Ag NPs induced by visible light ($\lambda < 550 \text{ nm}$) from what CQDs have converted, to promote photocharges further transportation. Indeed, 3S6CCN has a doubtless response to NIR region, which is much in evidence in Fig. 7f. The photocatalytic process over 3S6CCN is efficient with HER as 59.98 , 42.61 and $34.62 \mu\text{mol g}^{-1} \text{h}^{-1}$, even though for NIR light with 700 , 800 or 900 nm wavelength, respectively.

3.5. Proposed photocatalytic mechanism

The transient photocurrent responses were performed to investigate the charge transfer and separation conditions on pure $\text{g-C}_3\text{N}_4$, 6CCN and 3S6CCN composite photoelectrodes. Fundamentally, the reproducible curve shapes during four on-off illumination cycles provided in Fig. 8a validate the good photostability of these photocatalysts. It is noticeable that 6CCN displays relatively higher photocurrent density in comparison with that of bulk $\text{g-C}_3\text{N}_4$. Owing to the photocurrent derives from the migration of photogener-

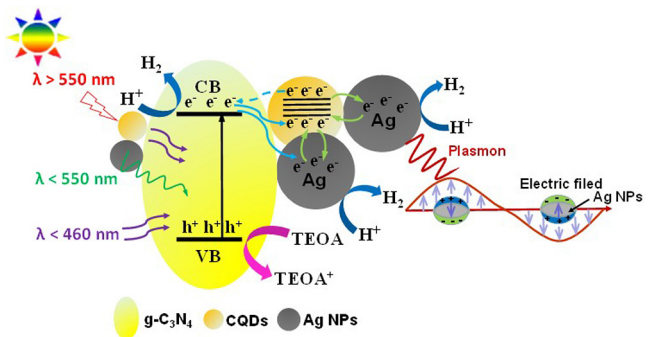


Fig. 9. Schematic presentation illustrating charge generation and transfer procedure over the Ag/CQDs/g-C₃N₄ composite combined with conjectural photocatalytic H_2 evolution mechanism.

erated electrons to the back contact, enhanced photocurrent value means that introducing CQDs is in favor of photoelectrons generation and transport [64,71]. Additionally, 3S6CCN exhibits the much stronger photocurrent intensity, which is about twofold as much as that of blank $\text{g-C}_3\text{N}_4$, demonstrating synergistic effect of CQDs and Ag NPs separate photogenerated electron-hole pairs more efficiently to minimize the recombination, which coincides with the PL results and photocatalytic activity measurements.

EIS Nyquist plots also provide another corroborative evidence for studying interfacial charge transfer behaviors of pure $\text{g-C}_3\text{N}_4$, 6CCN and 3S6CCN photoelectrodes (Fig. 8b). The front section akin to semicircle corresponds to charge transfer resistance and the smaller diameter signifies the weaker impedance and more efficient charge transfer [14,50]. The 3S6CCN has shown the best electronic conductivity with 6CCN taking second place, ascribed to the tight interface connection accomplished by addition of CQDs and Ag NPs [75], promoting the faster interfacial charge transfer and the improvement of photocatalytic performance.

On the basis of above analysis results, a tentative mechanism for light-driven aqueous protons reduction is put forward to account for the excellent photocatalytic activity over Ag/CQDs/g-C₃N₄ heterostructure (Fig. 9). The CQDs, Ag NPs and synergistic effect among every component play multiple important roles in the system. Under sunlight irradiation, only UV and visible light with wavelengths less than 460 nm could be absorbed by $\text{g-C}_3\text{N}_4$ matrix, then photogenerated electrons were excited from the valence band (VB) to the conduction band (CB), remaining positive holes created in the VB. While in the influence of LSPR effect-induced strong local electromagnetic fields, Ag NPs could act as the main force to aid Ag/CQDs/g-C₃N₄ system to capture photons with wavelengths shorter than 550 nm to an extreme, thereby elevating the quantity and formation speed of photo-excited $e_{\text{CB}}^- - h_{\text{VB}}^+$ pairs [44,76]. Simultaneously, long wavelengths ($\lambda > 550 \text{ nm}$) in solar light were up-converted to shorter wavelengths by the incorporated CQDs, which contributed to the succedent excitation of $\text{g-C}_3\text{N}_4$ or Ag/g-C₃N₄ system to form photoinduced carriers [56,67,76]. In reverse, SPR effect of Ag NPs generated from shorter wavelengths further promoted the light-harvesting capacity of CQDs as the photosensitizer. The holistic coordination, as it were, effectively harnessed the wide spectral (including NIR) region to ultimately achieve adequate utilization of solar energy.

Then, photo-excited electrons in the conduction band of $\text{g-C}_3\text{N}_4$ are thermodynamically available for H^+ reduction to liberate hydrogen [59]. In addition, the photoelectrons could rapidly migrate to CQDs and Ag NPs through the junction interface due to the matched band alignment [44,71]. Firstly, whether strong electromagnetic fields caused by SPR effect of Ag NPs or Mott-Schottky junction formed between Ag NPs and $\text{g-C}_3\text{N}_4$, accelerate the photoinduced electrons transport and electron-hole pairs separation of $\text{g-C}_3\text{N}_4$.

[7,76]. Besides, the electrons transferred to Ag NPs acquire more energy by electromagnetic fields, making themselves combined with H^+ to release H_2 more easily. Secondly, CQDs possess photoinduced electron-acceptance and electron-transfer properties, where they can trap redundant photoelectrons from $g\text{-}C_3N_4$ and Ag surface, also can transfer their electrons to $g\text{-}C_3N_4$ and Ag NPs, which may enhance the charge separation and protect the photocatalysts from photocorrosion to improve the stability of Ag/CQDs/ $g\text{-}C_3N_4$ nanocomposites [45,76]. Thirdly, both Ag NPs and CQDs can act as benign electron reservoirs utilizing their charge-storing advantage, facilitating electrons efficient extraction from the conduction band of $g\text{-}C_3N_4$ and impeding the recombination of the electron-hole pairs [44,52]. Finally, the coarsen surface and augmented surface area of Ag/CQDs/ $g\text{-}C_3N_4$ heterostructures provide sufficient active sites for reactant molecules [17,64]. Furthermore, during the photocatalytic process, the photo-generated holes of $g\text{-}C_3N_4$ can be reduced by sacrificial-agent TEOA for reutilization. In brief, the positive action rooted in mutual complement and cooperation of $g\text{-}C_3N_4$, CQDs and Ag NPs are dedicated to the enhancement of photocatalytic performance upon broad spectrum absorption.

4. Conclusions

A cluster of new-designed Ag/CQDs/ $g\text{-}C_3N_4$ complex photocatalysts have been successfully presented here by simple preparation and systematic characterization methods. It is the headmost report that the combination of SPR effect from Ag NPs with upconverted PL superiority of CQDs has devoted to $g\text{-}C_3N_4$ to implement the broad spectrum application, harnessing UV, visible and even near-infrared light for photocatalytic H_2 generation in aqueous solution. Besides, synergistic effect of Ag, CQDs and $g\text{-}C_3N_4$ at the benign contact interface can facilitate high-efficiency photoelectrons generation, transfer and separation, thereby improving the apparent quantum efficiency and photocatalytic capability. Among all the discussed photocatalysts above, the 3 wt% Ag/CQDs/ $g\text{-}C_3N_4$ hybrid system with excellent stability possesses the highest photocatalytic HER as $626.93\text{ }\mu\text{mol g}^{-1}\text{ h}^{-1}$ under visible light, which is a conspicuous enhancement in contrast to that of pure $g\text{-}C_3N_4$ and the optimal CQDs/ $g\text{-}C_3N_4$ composite. Hence, the novel Ag/CQDs/ $g\text{-}C_3N_4$ heterostructures could arouse inspiration and provide strategies for prospective broad-spectral photocatalysts design to generalize the utilization of clean energy.

Acknowledgements

We are extremely grateful to the National Natural Science Foundation of China (no. 21571064, 21371060), the fund of the Key Laboratory of Fuel Cell Technology of Guangdong Province and the Natural Science Foundation of Guangdong Province (S2013020013091) for financial support.

Appendix A. Supplementary data

Supplementary data associated with this article can be found, in the online version, at <http://dx.doi.org/10.1016/j.apcatb.2017.03.005>.

References

- [1] M.R. Gholipour, C.-T. Dinh, F. Béland, T.-O. Do, *Nanoscale* 7 (2015) 8208–8227.
- [2] T.-F. Yeh, S.-J. Chen, H. Teng, *Nano Energy* 12 (2015) 476–485.
- [3] T.-F. Yeh, C.-Y. Teng, S.-J. Chen, H. Teng, *Adv. Mater.* 26 (2014) 3297–3303.
- [4] A. Boudjemaa, A. Rebahi, B. Terfassa, R. Chebaut, T. Mokrani, K. Bachari, N. Coville, *Sol. Energy Mater. Sol. Cells* 140 (2015) 405–411.
- [5] T. Song, J.P. Huo, T. Liao, J. Zeng, J.Y. Qin, H.P. Zeng, *Chem. Eng. J.* 287 (2016) 359–366.
- [6] J.Y. Qin, J.P. Huo, P.Y. Zhang, J. Zeng, T.T. Wang, H.P. Zeng, *Nanoscale* 8 (2016) 2249–2259.
- [7] J. Zeng, T. Song, M.X. Lv, T.T. Wang, J.Y. Qin, H.P. Zeng, *RSC Adv.* 6 (2016) 54964–54975.
- [8] P.Y. Zhang, T.T. Wang, H.P. Zeng, *Appl. Surf. Sci.* 391 (2017) 404–414.
- [9] D.L. Jiang, Y. Zhang, H.Y. Chu, J. Liu, J. Wan, M. Chen, *RSC Adv.* 4 (2014) 16163–16171.
- [10] W.J. Wang, J. Yu, Z.R. Shen, D.L. Chan, T. Gu, *Chem. Commun.* 50 (2014) 10148–10150.
- [11] S. Patnaik, S. Martha, K.M. Parida, *RSC Adv.* 6 (2016) 46929–46951.
- [12] S.M. Yin, J.Y. Han, T.H. Zhou, R. Xu, *Sci. Technol.* 5 (2015) 5048–5061.
- [13] L.M. Sun, Y. Qi, C.-J. Jia, Z. Jin, W.L. Fan, *Nanoscale* 6 (2014) 2649–2659.
- [14] X.F. Chen, J. Wei, R.J. Hou, Y. Liang, Z.L. Xie, Y.G. Zhu, X.W. Zhang, H.T. Wang, *Appl. Catal. B Environ.* 188 (2016) 342–350.
- [15] X. Liu, X. Jian, H.M. Yang, H.Y. Dai, X.L. Song, Z.H. Liang, *Mater. Lett.* 176 (2016) 209–212.
- [16] Y.P. Zeng, Y. Wang, J.W. Chen, Y.W. Jiang, M. Kiani, B.Q. Li, R.L. Wang, *Ceram. Int.* 42 (2016) 12297–12305.
- [17] J. Tian, Y.H. Leng, Z.H. Zhao, Y. Xia, Y.H. Sang, P. Hao, J. Zhan, M.C. Li, H. Liu, *Nano Energy* 11 (2015) 419–427.
- [18] H.F. Shi, G.Q. Chen, C.L. Zhang, Z.G. Zou, *ACS Catal.* 4 (2014) 3637–3643.
- [19] Z. Zhu, Z.Y. Lu, D.D. Wang, X. Tang, Y.S. Yan, W.D. Shi, Y.S. Wang, N.L. Gao, X. Yao, H.J. Dong, *Appl. Catal. B Environ.* 182 (2016) 115–122.
- [20] Z. Zhu, X. Tang, C.C. Ma, M.S. Song, N.L. Gao, Y.S. Wang, P.W. Huo, Z.Y. Lu, Y.S. Yan, *Appl. Surf. Sci.* 387 (2016) 366–374.
- [21] J.L. Yuan, J.Q. Wen, Y.M. Zhong, X. Li, Y.P. Fang, S.S. Zhang, W. Liu, J. Mater. Chem. A 3 (2015) 18244–18255.
- [22] Y. Guo, J.H. Li, Z.Q. Gao, X. Zhu, Y. Liu, Z.B. Wei, W. Zhao, C. Sun, *Appl. Catal. B Environ.* 192 (2016) 57–71.
- [23] G. Miao, D.S. Huang, X.L. Ren, X. Li, Z. Li, J. Xiao, *Appl. Catal. B Environ.* 192 (2016) 72–79.
- [24] H. Liu, Z.Z. Xu, Z. Zhang, D. Ao, *Appl. Catal. B Environ.* 192 (2016) 234–241.
- [25] M. Faisal, A. Ismail, F. Harraz, S. Al-Sayari, A.M. El-Toni, M. Al-Assiri, *Mater. Des.* 98 (2016) 223–230.
- [26] Z.-A. Lan, G.G. Zhang, X.C. Wang, *Appl. Catal. B Environ.* 192 (2016) 116–125.
- [27] B. Chai, X. Liao, F.K. Song, H. Zhou, *Dalton Trans.* 43 (2014) 982–989.
- [28] X.H. Zhang, T.Y. Peng, L.J. Yu, R.J. Li, Q.Q. Li, Z. Li, *ACS Catal.* 5 (2015) 504–510.
- [29] J.-P. Zou, L.-C. Wang, J.M. Luo, Y.-C. Nie, Q.-J. Xing, X.-B. Luo, H.-M. Du, S.-L. Luo, S. Suib, *Appl. Catal. B Environ.* 193 (2016) 103–109.
- [30] Q. Liu, T.X. Chen, Y.R. Guo, Z.G. Zhang, X.M. Fang, *Appl. Catal. B Environ.* 193 (2016) 248–258.
- [31] S. Bera, J.E. Lee, S.B. Rawal, W.I. Lee, *Appl. Catal. B Environ.* 199 (2016) 55–63.
- [32] X. Lin, B. Wei, X.X. Zhang, M.S. Song, S.Y. Yu, Z.Y. Gao, H.J. Zhai, L. Zhao, G.B. Che, *Sep. Purif. Technol.* 169 (2016) 9–16.
- [33] Y.H. Lee, D.H. Kim, T.W. Kim, *Org. Electron.* 37 (2016) 74–79.
- [34] K.H. Leong, S.L. Liu, L.C. Sim, P. Saravanan, M. Jang, S. Ibrahim, *Appl. Surf. Sci.* 358 (2015) 370–376.
- [35] S.L. Ma, S.H. Zhan, Y.A. Jia, Q. Shi, Q.X. Zhou, *Appl. Catal. B Environ.* 186 (2016) 77–87.
- [36] S.T. Ren, G.L. Zhao, Y.Y. Wang, B.Y. Wang, Q. Wang, *Nanotechnology* 26 (2015) 125403–125412.
- [37] T.J. Chen, W. Quan, L.B. Yu, Y.Z. Hong, C.J. Song, M.S. Fan, L.S. Xiao, W. Gu, W.D. Shi, J. *Alloys Compd.* 686 (2016) 628–634.
- [38] M.J. Muñoz-Batista, O. Fontelles-Carceller, M. Ferrer, M. Fernández-García, A. Kubacka, *Appl. Catal. B Environ.* 183 (2016) 86–95.
- [39] Y.J. Sun, T. Xiong, Z.L. Ni, J. Liu, F. Dong, W. Zhang, W.-K. Ho, *Appl. Surf. Sci.* 358 (2015) 356–362.
- [40] Y.-Z. Wang, N. Hao, Q.-M. Feng, H.-W. Shi, J.-J. Xu, H.-Y. Chen, *Biosens. Bioelectron.* 77 (2016) 76–82.
- [41] S. Vadivel, V. Kamalakkannan, N. Kavitha, T.S. Priya, N. Balasubramanian, *Mater. Sci. Semicond. Process.* 41 (2016) 59–66.
- [42] D.M. Chen, Z.H. Wang, Y. Du, G.L. Yang, T.Z. Ren, H. Ding, *Catal. Today* 258 (2015) 41–48.
- [43] Y.G. Su, Y.X. Zhao, Y.J. Zhao, J.Y. Lang, X. Xin, X.J. Wang, *Appl. Surf. Sci.* 358 (2015) 213–222.
- [44] J. Liu, H.C. Zhang, D. Tang, X. Zhang, L.K. Yan, Y.Z. Han, H. Huang, Y. Liu, Z.H. Kang, *ChemCatChem* 6 (2014) 2634–2641.
- [45] J. Wang, Y.H. Ng, Y.-F. Lim, G.W. Ho, *RSC Adv.* 4 (2014) 44117–44123.
- [46] Y. Guo, P.J. Yao, D.Q. Zhu, C. Gu, J. Mater. Chem. A 3 (2015) 13189–13192.
- [47] X.H. Gao, Y.Z. Lu, R.Z. Zhang, S.J. He, J. Ju, M.M. Liu, L. Li, W. Chen, J. Mater. Chem. C 3 (2015) 2302–2309.
- [48] M. Jahanbakhshi, B. Habibi, *Biosens. Bioelectron.* 81 (2016) 143–150.
- [49] S.S. Liu, H.J. Cao, Z.Y. Wang, W.W. Tu, Z.H. Dai, *Chem. Commun.* 51 (2015) 14259–14262.
- [50] F.W. Ming, J.Q. Hong, X. Xu, Z.C. Wang, *RSC Adv.* 6 (2016) 31551–31558.
- [51] M. Amjadi, Z. Abolghasemi-Fakhri, T. Hallaj, *J. Photochem. Photobiol. A* 309 (2015) 8–14.
- [52] H.J. Yu, Y.F. Zhao, C. Zhou, L. Shang, Y. Peng, Y.H. Cao, L.-Z. Wu, C.-H. Tung, T.R. Zhang, *J. Mater. Chem. A* 2 (2014) 3344–3351.
- [53] X. Zhang, F. Wang, H. Huang, H.T. Li, X. Han, Y. Liu, Z.H. Kang, *Nanoscale* 5 (2013) 2274–2278.
- [54] X. Han, Y.Z. Han, H. Huang, H.C. Zhang, X. Zhang, R.H. Liu, Y. Liu, Z.H. Kang, *Dalton Trans.* 42 (2013) 10380–10383.
- [55] H.T. Li, R.H. Liu, Y. Liu, H. Huang, H. Yu, H. Ming, S.Y. Lian, S.-T. Lee, Z.H. Kang, *J. Mater. Chem.* 22 (2012) 17470–17475.
- [56] J.G. Hou, H.J. Cheng, C. Yang, O. Takeda, H.M. Zhu, *Nano Energy* 18 (2015) 143–153.

[57] M.X. Ji, J.X. Xia, J. Di, B. Wang, S. Yin, L. Xu, J.Z. Zhao, H.M. Li, *J. Colloid Interface Sci.* 478 (2016) 324–333.

[58] B.M. Martindale, G.M. Hutton, C. Caputo, E. Reisner, *J. Am. Chem. Soc.* 137 (2015) 6018–6025.

[59] J. Liu, Y. Liu, N.Y. Liu, Y.Z. Han, X. Zhang, H. Huang, Y. Lifshitz, S.-T. Lee, J. Zhong, Z.H. Kang, *Science* 347 (2015) 970–974.

[60] S. Fang, Y. Xia, K.L. Lv, Q. Li, J. Sun, M. Li, *Appl. Catal. B Environ.* 185 (2016) 225–232.

[61] K. Li, F.-Y. Su, W.-D. Zhang, *Appl. Surf. Sci.* 375 (2016) 110–117.

[62] R.H. Liu, H. Huang, H.T. Li, Y. Liu, J. Zhong, Y.Y. Li, S. Zhang, *ACS Catal.* 4 (2014) 328–336.

[63] L.M. Shen, M.L. Chen, L.L. Hu, X.W. Chen, J.H. Wang, *Langmuir* 29 (52) (2013) 16135–16140.

[64] J.P. Huo, H.P. Zeng, *J. Mater. Chem. A* 3 (2015) 17201–17208.

[65] X.J. Bai, R.L. Zong, C.X. Li, D. Liu, Y.F. Liu, Y.F. Zhu, *Appl. Catal. B Environ.* 147 (2014) 82–91.

[66] W.-J. Ong, L.-L. Tan, Y.H. Ng, S.-T. Yong, S.-P. Chai, *Chem. Rev.* 116 (2016) 7159–7329.

[67] L.T. Ma, H.Q. Fan, J. Wang, Y.W. Zhao, H.L. Tian, G.Z. Dong, *Appl. Catal. B Environ.* 190 (2016) 93–102.

[68] H.M. Lv, J.Y. Shen, J.X. Wang, Z.S. Cui, J.M. Xie, *RSC Adv.* 5 (2015) 15993–15999.

[69] Y.X. Yang, Y.N. Guo, F.Y. Liu, X. Yuan, Y.H. Guo, S.Q. Zhang, W. Guo, M.X. Huo, *Appl. Catal. B Environ.* 142–143 (2013) 828–837.

[70] Y.X. Li, S.X. Ouyang, H. Xu, X. Wang, Y.P. Bi, Y.F. Zhang, J.H. Ye, *J. Am. Chem. Soc.* 138 (2016) 13289–13297.

[71] H. Zhang, L.X. Zhao, F.L. Geng, L.-H. Guo, B. Wan, Y. Yang, *Appl. Catal. B Environ.* 180 (2016) 656–662.

[72] J. Jin, Q. Liang, C.Y. Ding, Z.Y. Li, S. Xu, *J. Alloys Compd.* 691 (2017) 763–771.

[73] O. Fontelles-Carceller, M.J. Muñoz-Batista, M. Fernández-García, A. Kubacka, *ACS Appl. Mater. Interfaces* 8 (2016) 2617–2627.

[74] X.Y. Xu, Z.J. Bao, G. Zhou, H.B. Zeng, J.G. Hu, *ACS Appl. Mater. Interfaces* 8 (2016) 14118–14124.

[75] J. Di, J.X. Xia, M.X. Ji, B. Wang, S. Yin, H. Xu, Z.G. Chen, H.M. Li, *Langmuir* 32 (2013) 2075–2084.

[76] H.C. Zhang, H. Huang, H. Ming, H.T. Li, L.L. Zhang, Y. Liu, Z.H. Kang, *J. Mater. Chem.* 22 (2012) 10501–10506.